Ayame Ikeda[1], Hiroyuki Kumagai[1], and Tomokatsu Morota[2]

[1]Graduate School of Environmental Sciences, Nagoya University, Nagoya, Japan

[2]Graduate School of Science, The University of Tokyo, Tokyo, Japan

Corresponding author: Ayame Ikeda (ikeda.ayame@k.mbox.nagoya-u.ac.jp)

Key Points:

- Distributions of boulder falls, small craters, and optical maturity values on lunar crater walls were correlated with crater slope angles.
- Boulder falls were triggered by small meteorite impacts near boulders rather than by shallow moonquakes.
- We proposed a model for the generation and transport of boulders and regolith on crater walls resulting in the degradation of craters.

Abstract

Recent explorations by lunar orbiters have shown that boulder falls are distributed over the entire lunar surface. To quantitatively evaluate the effects of moonquakes and meteorite impacts on boulder falls, we performed detailed surveys at two sites: one in the southern part of the Schrödinger basin (Site 1) and the other in Laue crater (Site 2). Using images and topography data from the Lunar Reconnaissance Orbiter and KAGUYA, we estimated the detailed distributions of boulder falls, small craters, slope angles, the optical maturity parameter (OMAT), and maximum acceleration due to impacts at these sites. In steeply sloping areas at both sites, we found that the density of small craters was small and areas with high OMAT values corresponded to boulder sources, where many boulders exist. At Site 1, the starting points of boulder falls and acceleration due to impacts were correlated. In addition, craters with boulder falls at and around Site 2 were distributed independently of the epicentral distance from a shallow moonquake that occurred in 1975 near Site 2, which was previously inferred to have triggered boulder falls at the site. Our results suggest that boulder falls at these sites were triggered not by moonquakes but by meteorite impacts. We propose a model for the generation and transport of boulders and regolith on slopes by meteorite impacts, which may be directly related to the degradation of crater slopes on the Moon.

Plain Language Summary

Large rocks (a few to tens of meters in size) or boulders with accompanying trails on crater slopes have been widely found on the Moon from high-resolution images taken by recent lunar orbiters. These observations indicate that crater slopes experienced large ground shaking that triggered boulder falls. There are two ideas to explain how boulder falls occurred: one by seismic events or moonquakes and the other by meteorite impacts. In order to investigate the cause of boulder falls, we performed detailed analysis of image data at two sites, where boulders and boulder falls were found on slopes of large craters. Our

results show that there are many boulders in steeply sloping areas near the edges of the large craters, where fresh materials are exposed. We found that the starting points of boulder falls exist in large shaking areas during meteorite impacts that produced small craters on the slopes, but no clear evidence to support that boulder falls were triggered by moonquakes. These results indicate that boulders were generated in the upslope areas and their falls were triggered by meteorite impacts. Our findings contribute to understand how topography changes with the movement of rocks and soil on crater slopes.

1. Introduction

Mass wasting, which occurs over the entire surface of the Moon, is fundamental to understanding topographic degradation and recent near-surface activity on the Moon (e.g., Xiao et al., 2013). Although our understanding of the physical mechanisms of mass-wasting phenomena such as rock or boulder falls and landslides on the lunar surface have been hindered by limited observations, recent explorations by lunar orbiters have improved our knowledge of mass-wasting processes. The Japanese lunar orbiter SELENE, which is known in Japan by its nickname KAGUYA, is equipped with a multi-band imager, laser altimeter, and terrain camera and provided global image data during 2007−2009 that clarified the detailed topography of the entire lunar surface (Araki et al., 2009; Haruyama et al., 2008) and the compositions of lunar rocks (Ohtake et al., 2009). The Lunar Reconnaissance Orbiter (LRO) operated by NASA from 2009 to the present has provided high-resolution images taken by the Lunar Reconnaissance Orbiter Camera (LROC) (Robinson et al., 2010) in which small topographic features such as lobate scarps and boulder falls can be identified (e.g., Kumar et al., 2016; Watters et al., 2010). The huge LROC image data archive has been analyzed by using a deep learning approach to estimate global boulder distributions (e.g., Bickel et al., 2020) and temporal topographic changes by comparing images taken at different times (e.g., Robinson et al., 2015). Lobate scarps, which are widely distributed on the lunar surface (Watters et al., 2015, 2019), may be formed by tidal stresses (Watters et al., 2019) or contraction of the Moon (Watters et al., 2010). Boulders and boulder falls with accompanying trails (e.g., Kumar et al., 2016; 2019) have been identified across the lunar surface, especially on crater walls (Bickel et al., 2020, 2021).

Kumar et al. (2016) investigated the detailed distribution of boulder falls in the southern part of the Schrödinger basin, about 8 km from nearby lobate scarps. Kumar et al. (2019) studied an area in Laue crater, where a shallow moonquake was recorded on 3 January 1975 by the Apollo lunar seismograph network (Nakamura et al., 1979). Mohanty et al. (2020) mapped boulder falls in the Orientale basin, where abundant tectonic structures such as normal faults along basin rings and grabens are found. They concluded that, in these areas, shallow moonquakes at lobate scarps and tectonic faults triggered boulder falls. However, it is not known whether lobate scarps are active faults that generate moonquakes radiating high-frequency seismic waves and triggering boulder falls. Kokelaar et al. (2017) and Houston et al. (1973) noticed that ground shak-

ing due to impacts is an important contributor to mass wasting on the Moon. Xiao et al. (2013) indicated that mass wasting can be triggered by both impact cratering and moonquakes, and that cratering induces seismic shock waves and crushes subsurface bedrock, causing the formation of fractured zones beneath the crater floor. Xiao et al. (2013) also noted that when moonquakes occur repeatedly, the accumulated damage may promote various mass-wasting phenomena, even though a single moonquake may not be strong enough to cause mass wasting. Bickel et al. (2020, 2021) suggested that impacts during the Late Heavy Bombardment event, about 3.9 billion years ago (e.g., Head et al., 2010; Tera et al., 1974), fractured the bedrock, and the resultant rock fragments have been brought to the lunar surface as boulders over billions of years by continuous meteorite impacts. Kumar et al. (2019) inferred that a single moonquake triggered boulder falls in Laue crater, but they did not quantitatively evaluate ground shaking due to impacts in their studies (Kumar et al., 2016, 2019).

Boulder falls provide invaluable information on how ground shaking occurs on the Moon, and this information is fundamentally important in investigations of dynamic processes associated with mass wasting. In this study, we quantitively evaluated the effects of both moonquakes and meteorite impacts on boulder falls in the two areas studied by Kumar et al. (2016, 2019) to improve understanding of the physical mechanisms of mass-wasting processes. Using images obtained by the LRO and KAGUYA, we systematically estimated the distributions of boulder falls, impact craters, and associated ground shaking, slope angles, and the optical maturity parameter (OMAT) at the two sites. The results of our comparison of these distributions strongly suggest that boulder falls at our study sites were caused by small impacts on crater slopes. Considering these results, we propose a model for the formation and downslope movement of boulders and regolith by such impacts that can explain the degradation of crater slopes at not only these sites but also other crater sites on the Moon.

2. Study Areas, Data, and Methods

We explored two sites (Sites 1 and 2; Figure 1) previously studied by Kumar et al. (2016, 2019). Site 1 (5 km NS × 7 km EW) is located on the inner southern wall of the Schrödinger basin (79.35°−79.48°S, 128.4°−129.5°E), which is near the South Pole–Aitken basin, the largest basin on the Moon. Lobate scarps occur to the north of Site 1; the closest one is 8 km from our study area (Figure 1b). Site 2 is a small crater (28.5°−29°N, 262.5°−263°E; diameter 8 km) located on the floor of Laue crater. Lobate scarps are located on the Lorentz basin wall to the south of Site 2 (Kumar et al., 2019) (Figure 1c). Kumar et al. (2019) inferred that a moonquake with a seismic moment magnitude (M_w) of 4.1 occurred on 3 January 1975 along the longest lobate scarp segment (Figure 1c).

We measured boulder falls and small craters on images obtained by the LRO Narrow Angle Camera (NAC), which captured optical black and white images with a resolution of 0.5 m/pixel (Robinson et al., 2010). We also used digital terrain model (DTM) data created from stereo images taken by the terrain camera (TC; resolution 10 m/pixel, Haruyama et al., 2008) onboard KAGUYA

to estimate slope angles, and we used multi-band image data from the multi-band imager (MI) onboard KAGUYA to estimate OMAT values. The MI data comprise nine bands in the 415−1000 nm (VIS) and 1000−1550 nm (NIR) wavelength ranges (Ohtake et al., 2009) with resolutions of 20 m (VIS) and 62 m (NIR). The images and topographic data used in this study are listed in Table 1.

Surface age was estimated by the crater counting method, which uses the crater size–frequency distribution (CSFD), which was assumed to be stable over time, and the cratering chronology model derived from the relationship between crater density and the radiometric ages of lunar samples (Neukum, 1983; Neukum et al., 2001). We used the CSFD described by the following production function (Neukum, 1983):

,

where D is the crater diameter (km), $N(D)$ is the cumulative number of craters with diameter larger than D per unit area (km^{-2}), and a_0−a_{11} are polynomial coefficients (see Neukum, 1983, for the coefficient values). The crater chronology function is as follows (Neukum, 1983):

,

where $N(1)$ is the cumulative number of craters with $D = 1$ km and T is time (Gyr). We used the Craterstats software (Michael & Neukum, 2010) and equations (1) and (2) to determine surface ages in the study areas.

To estimate the peak ground acceleration (PGA, cm/s^2) induced by meteorite impacts and moonquakes, we used the following attenuation equation for earthquakes (Kanno et al., 2006):

,

where X is epicentral distance (km). This equation was derived from strong-motion records of earthquakes with $M_w > 5.5$ occurring during 1996−2003 in Japan and other countries. We extrapolated this equation for small meteorite impacts and moonquakes, where PGA was normalized by the lunar gravitational acceleration ($g = 1.62$ m/s^2). Although faulting that generates seismic waves is considered to be identical between moonquakes and earthquakes, seismic structural differences, especially in intrinsic and scattering attenuations (Q_i^{-1} and Q_s^{-1}, respectively), between the Moon and Earth may result in different seismic wave attenuations between moonquakes and earthquakes. Q_i values in the upper mantle and crust of the Moon and Earth have been estimated to be more than 4000 (Nakamura & Koyama, 1982) and about 100−500 (Dziewonski & Anderson, 1981), respectively, indicating that intrinsic attenuation is relatively small on the Moon. On the other hand, total scattering coefficients (g_0) around a frequency (f) of 1 Hz are 1−2 orders larger on the Moon (about 10^{-3} m^{-1}) than on the Earth (about 10^{-5} m^{-1}) (Sato et al., 2012). Accordingly, $Q_s = 2\,f$ $/(g_0\ )$ with an S-wave velocity ( ) of 3000 m/s is estimated to be 2 on the Moon and 200 on Earth; thus, scattering attenuation is relatively large on the Moon.

Therefore, equation (3) may not be suitable for estimating absolute PGA values but can be used to estimate relative values within small hypocentral distances, where intrinsic and scattering attenuation effects are considered to be small.

Table 1. Images and topographic data used in this study.

	Site 1	Site 2
LROC	M154370363LC	M1097122291LC
NAC	M1390708014LC	M1244314600RC
	M141446269LC	M1206659832RC
	M139071213LC	M1206659832LC
KAGUYA	MI_MAP_03_S79E128S80E129SC	MI_MAP_03_N29E262N28E263SC
	MI_MAP_03_S79E129S80E130SC	DTM_MAPs02_N30E261N27E264SC
	MI_MAP_03_S79E130S80E131SC	
	DTM_MAPs02_S78E129S81E132SC	

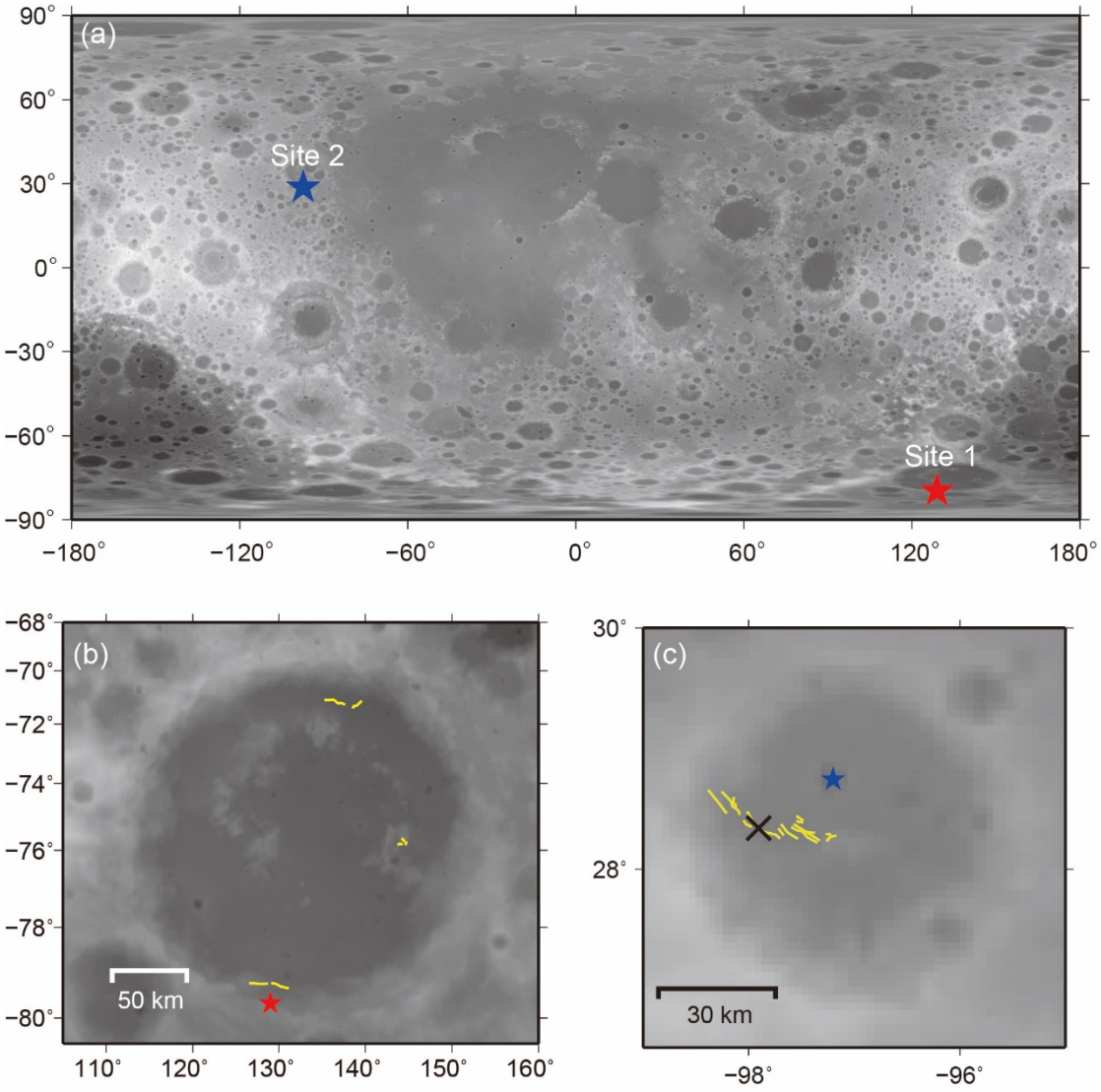

Figure 1. (a) Topography of the Moon and the locations of Sites 1 and 2 (red and blue star, respectively). (b) Site 1 (red star) and lobate scarps (yellow lines) in the Schrödinger basin. (c) Site 2 (blue star), lobate scarps (yellow lines), and the epicenter assumed by Kumar et al. (2019) for a moonquake on 3 January 1975 (black cross) in Laue crater.

We used the following relationship between crater diameter (D, m) and the seismic moment (M_0, Nm) derived by Teanby and Wookey (2011):

,

where $a = 8.8 \times 10^{-3}$, $b = 0.32$, $c = 4.8 \times 10^{-9}$, $d = 1.24$, k is the seismic

efficiency (2.0×10^{-5}), and g_e is gravitational acceleration on the Earth. We converted M_0 to M_w by using the following equation (Kanamori, 1977):

.

We first used equations (4) and (5) to estimate M_w values for the meteorite impacts that created individual small craters. Then, using equation (3), we calculated PGA values from M_w values of meteorite impacts at individual points in each study area. We set the epicenter at the center of each small crater, and used the PGA at the crater rim for acceleration within the crater. We adopted the maximum acceleration at each point among PGA values calculated for all small craters.

Space weathering, mainly due to the solar wind, causes lunar surface optical features to become darker and redder and can be evaluated by OMAT (Lucey et al, 1995, 2000; Otake et al., 2012), obtained by using the following equation:

,

where R_{750} and R_{950} are reflectance values at wavelengths of 750 nm and 950 nm, respectively. Thus, high OMAT values indicate a fresh surface. We estimated OMAT values from MI data in these two bands obtained by KAGUYA.

We used ENVI 5.6 software to generate map-projected LROC NAC and KAGUYA mosaic images, on which we traced boulder trails and small craters and calculated OMAT values. We inferred starting points of boulder falls from our trail traces. Some trails could not be clearly traced because of degradation by subsequent mass wasting; in such cases, we determined the highest point of each trail. We measured the diameters of small craters by assuming that they were circular. We also used SAOImageDS9 software (Joye & Mandel, 2003) to map small craters, boulder trails, and boulder sources. We used Generic Mapping Tools (GMT) (Wessel & Smith, 1998) to calculate the direction of the upslope gradient vector and the magnitude of the gradient scalar and to map lunar topography, slope gradients, distributions of small craters, boulder trails and sources, and PGA distributions.

3. Results

3.1. Site 1 in the Schrödinger Basin

Our estimated locations of small impact craters (D 5 m) and their diameters and boulder trail locations at Site 1 in the Schrödinger basin are shown in Figure 2a. Many boulders are located in upslope areas near the basin rim (areas enclosed by green lines in Figure 2a). Such areas are called boulder sources by Kumar et al. (2016). Some boulders had moved downslope, leaving trails (Figure 2c). Older trails are superimposed by small impact craters, whereas younger trails crosscut craters (Figure 2a, yellow and green lines, respectively). Our detected boulder trails and boulder sources are mostly consistent with those detected by Kumar et al. (2016). Small craters and boulder trails are not uniformly distributed in our study area. Boulder trails are more abundant in

the central region than in the NW and SE regions (Figure 2a), but the density of small craters is larger in the NW and SE regions than in the central region (Figure 2b). In some areas below the boulder sources (enclosed by blue lines in Figure 2a), there are fewer small craters and boulder trails. We estimated the mean surface model age at Site 1 to be about 5.5 Ma, based on the CSFD of small impact craters ranging from 10 to 200 m in diameter (Figure S1a). It is clear that crater density is smaller in the study area than on the basin floor and the outer part of the basin rim (north and south of the study area, respectively); thus, the study area is younger than surrounding areas.

Using equation (3) and the procedure described in Section 2, we estimated the spatial distribution of maximum acceleration due to impacts and compared the result with the estimated starting points of boulder falls (Figure 3). Many starting points of boulder falls were found in areas where the acceleration due to impacts was large, especially in the central part of our study area. To consider the relationship between maximum acceleration and boulder fall starting points quantitatively, we subdivided the study area into 600 m $\times$ 600 m grids, and then averaged the maximum acceleration and counted the number of starting points within each grid (Figure S2a). We found that the relationship between the averaged maximum acceleration and the number of starting points differed among three regions (regions 1 to 3 in Figure S2). The relationship is clearest in region 2 (magenta rectangle in Figure 3; Figure 4a) and less clear in regions 1 and 3 (Figures S2b and S2d, respectively). In region 2, the number of starting points increases with increasing averaged acceleration (correlation coefficient $R = 0.58$; Figure 4a). In regions 1 and 3, there are fewer boulder trails than in region 2, but small craters are more abundant (Figure 3). These differences among the regions may be attributable to the further progression of slope degradation in regions 1 and 3, which are older than region 2. We discuss this point later.

We also compared the mean slope angle with the density of small craters in each of the three regions (Figure S3a). Most small craters are in downslope and upslope areas, where slope angles are relatively small (Figures 2b and S3a), and the density of small craters tends to decrease as the slope angle ($>25°$) increases (Figure 4b). This tendency is weaker where slope angles are gentle ($<25°$) because Site 1 was selected as a relatively steeply sloping area along the basin wall; as a result, there are few data points in gently sloping areas.

Comparison of estimated OMAT values with boulder source areas (enclosed by solid gray lines in Figure 5a) showed large OMAT values, which were mainly associated with upslope areas, to be highly correlated with boulder source areas. This result indicates that boulder source areas are characterized by relatively fresh materials. Moreover, OMAT values decrease downslope (Figure 5a), indicating that soils are more mature in downslope areas. Comparison of average OMAT values in 230 m $\times$ 230 m grids with the density of small craters in the grids showed that small crater density decreases as OMAT values increase (Figure 4c); this trend is similar to that found between small crater density and slope angle (Figure 4b). Comparison of OMAT values with slope angles (Figure

4d) indicated that the smallest OMAT value for each slope angle systematically increases with increasing slope angle, whereas larger OMAT values show more scatter, although they tend to increase as the slope angle increases. These features suggest that the maturity of the crater wall surface is related to the slope angle.

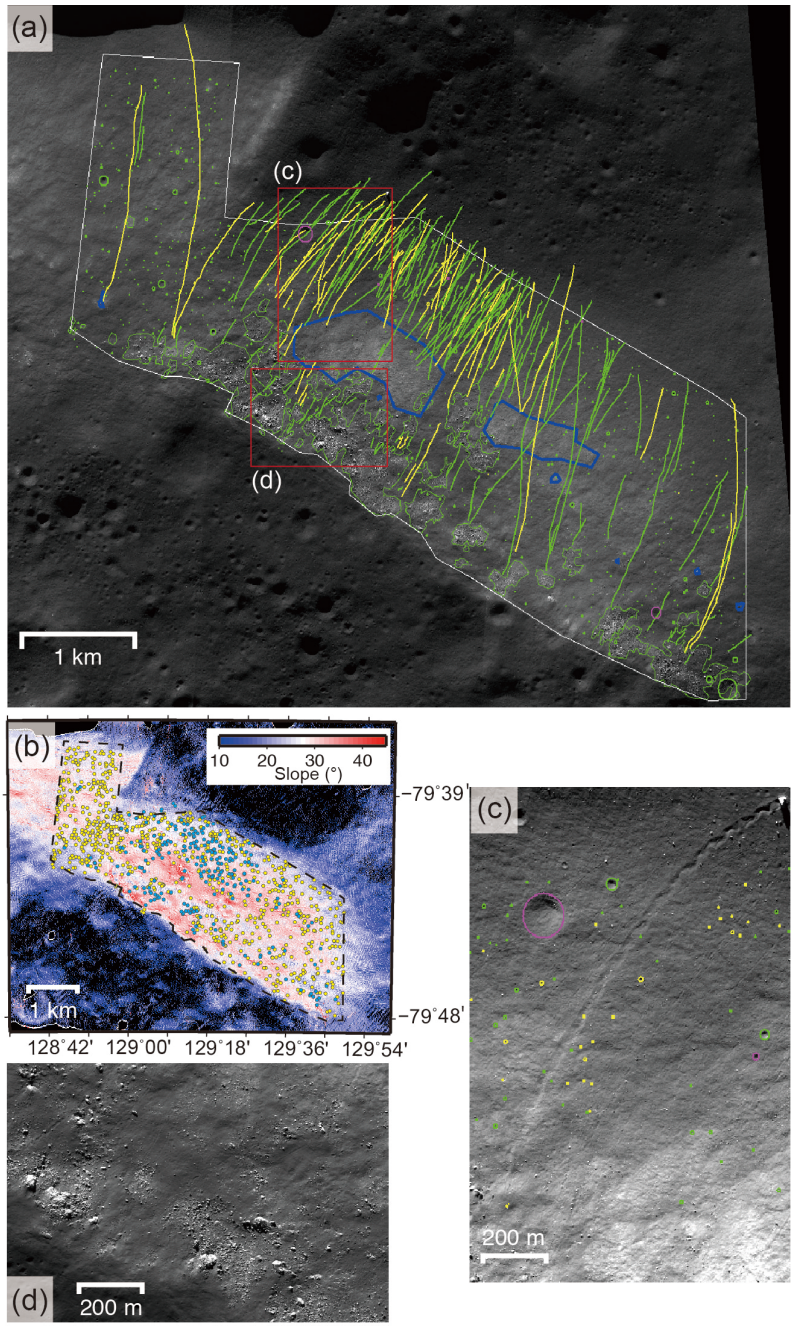

Figure 2. (a) LROC NAC image mosaic (M154370363LC, M141446269LC, and M139071213LC) of Site 1 (downslope is northeastward) with boulder source areas (enclosed by green lines), boulder trails (green and yellow lines), and

small craters ($D > 5$ m) in the study area (enclosed by the white line). Craters superimposed by boulder trails and those crosscut by boulder trails are shown by red and yellow circles, respectively; other craters are indicated by green circles. The areas enclosed by blue lines indicate those without boulders, boulder falls, and small craters below the boulder sources. (b) Distributions of slope angles estimated from KAGUYA topographic data at Site 1. Locations of small craters in the study area (within the black dashed line) are shown by yellow circles, and starting points of boulder falls are shown by cyan circles. Enlarged views of (c) boulder trails and small craters and (d) boulder source areas, within the red rectangles in (a).

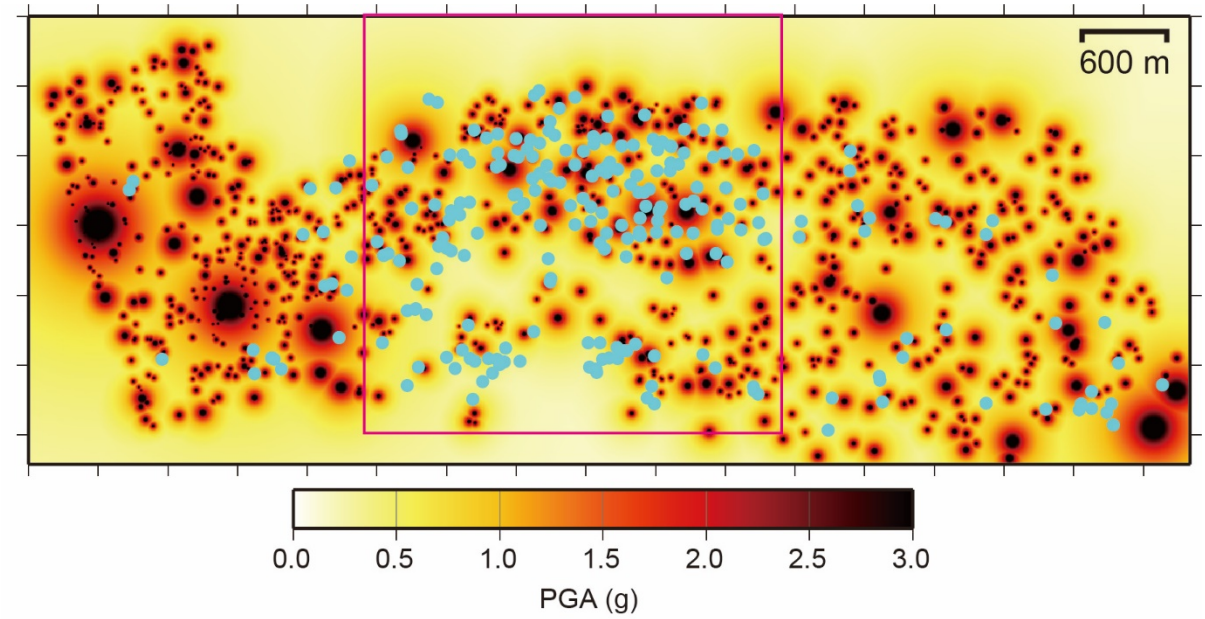

Figure 3. Spatial distributions of starting points of boulder falls (cyan circles) and maximum peak ground acceleration (PGA) due to meteorite impacts (color scale) at Site 1. The region with the strongest correlation between starting points and maximum acceleration is within the magenta rectangle (region 2 in Figure S2).

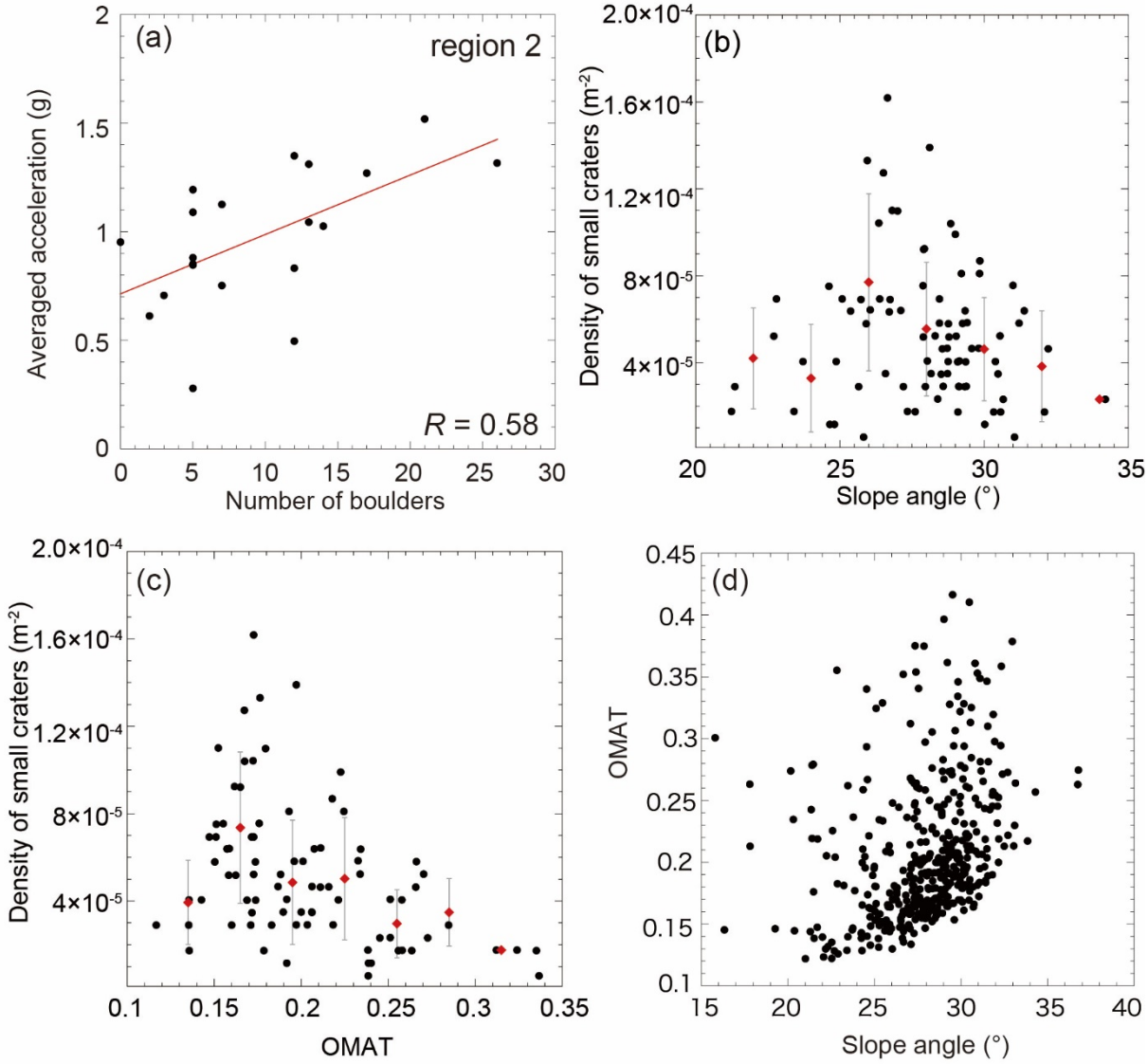

Figure 4. Relationships among various parameter values at Site 1. (a) Averaged maximum acceleration versus the number of starting points of boulder falls with the best-fit linear relation (red line). (b) Density of small craters versus mean slope angle. (c) Density of small craters versus averaged OMAT value. (d) Mean slope angle versus averaged OMAT value. Parameters were calculated within grids with dimensions of 600 m × 600 m in (a), about 450 m × 450 m in (b) and (c), and 230 m × 230 m in (d). Red diamonds and associated error bars in (b) and (c) show the average and standard deviation of the density of small craters in individual 2° slope angle bins and 0.02 OMAT bins, respectively.

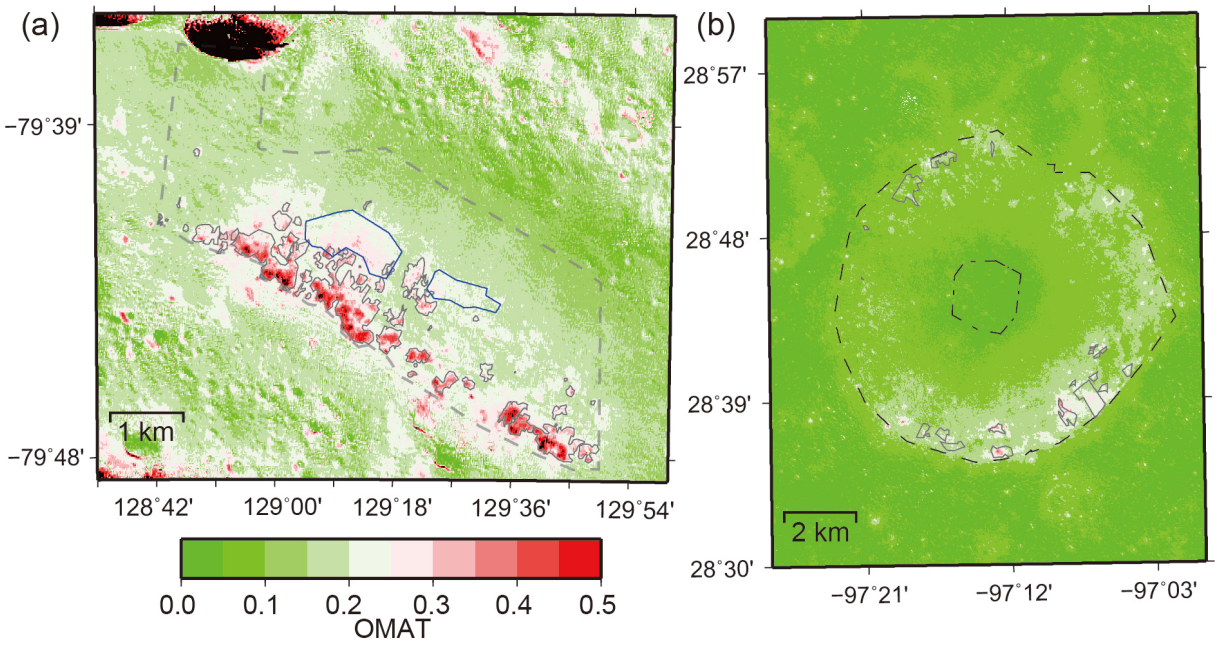

Figure 5. Spatial distributions of OMAT values (color scale) and boulder source areas (enclosed by solid gray lines) at (a) Site 1 and (b) Site 2. The study area at each site is enclosed by dashed lines. The areas enclosed by blue lines in (a) correspond to those in Figure 2a. The dash-dotted line in (b) encloses the crater floor.

3.2. Site 2 in Laue Crater

At Site 2, we measured boulder trails and small craters ($D > 15$ m) and their distributions along the entire crater wall and on the floor of Laue crater (Figure 6a). Boulder trails occur only on the southeast and northwest walls, and fewer boulder trails are superimposed by small craters (yellow lines in Figure 6a) at Site 2 than at Site 1 (see Figure 2a). Our measured locations of boulder trails and boulder sources are mostly consistent with those of Kumar et al. (2019), but we identified fewer boulder trails than Kumar et al. (2019) did. Comparison of the distributions of slope angles, small craters, and starting points of boulder falls indicate that at Site 2 there are fewer small craters in areas where slope angles are larger than about 30° than in areas with smaller slope angles (Figure 6b).

We selected one area with boulder trails (red rectangle in Figure 6a) and compared the spatial distribution of maximum acceleration due to impacts with the starting points of boulder falls within that area (Figure 7). Although the averaged maximum acceleration in 500 m× 500 m grids (Figure S6) was weakly correlated with the number of starting points (Figure 8a), their correlation was weaker than that at Site 1 (Figure 4a).

The model age estimated by using all measured small craters with diameters of 15−500 m at Site 2 was about 20 Ma (Figure S5a), but when only small craters on the eastern and western walls were used, the estimated model ages were about 13 and 14 Ma, respectively, and the estimated model age of the crater floor was about 70 Ma (Figure S5b). These results show that the Laue crater walls are relatively younger than its floor. We averaged slope angles and estimated the density of small craters in 800 m × 900 m grids at Site 2 (Figure S3b), and found that, similar to the trend at Site 1 (Figure 4b), the density of small craters at Site 2 decreases with increasing slope angle (Figure 8b).

OMAT values are high mainly in the southeast and northwest upslope areas at Site 2 (Figure 5b), and similar to Site 1 (Figure 5a), high values are correlated with boulder sources. OMAT values decrease toward the crater floor (Figure 5b), indicating more mature soils. We also compared OMAT values with small crater density (Figure 8c) and slope angle (Figure 8d) at Site 2. Although we found no clear correlation between OMAT and the density of small craters, OMAT values tend to increase with slope angle at Site 2, similar to the tendency at Site 1 (Figure 4d).

Kumar et al. (2019) inferred that boulder falls at Site 2 were triggered by a shallow M_w 4.1 moonquake that occurred on 3 January 1975. The epicenter, as originally determined by Nakamura et al. (1979) and relocated by Kumar et al. (2019), was on the largest lobate scarp segment. We investigated boulder falls in other craters ($D > 7$ km) around Site 2 within an epicentral distance of about 200 km from the moonquake (Figure 9a) and found boulder falls in some craters far from the epicenter. We then estimated the number of craters per unit area whose centers were within a radius of 70, 140, or 210 km from the moonquake epicenter (Figure 9b), but we did not find any dependence of the number of craters either with or without boulder falls on epicentral distance. This result is consistent with the findings of Bickel et al. (2021), who statistically analyzed the global distributions of boulder falls and moonquake epicenters.

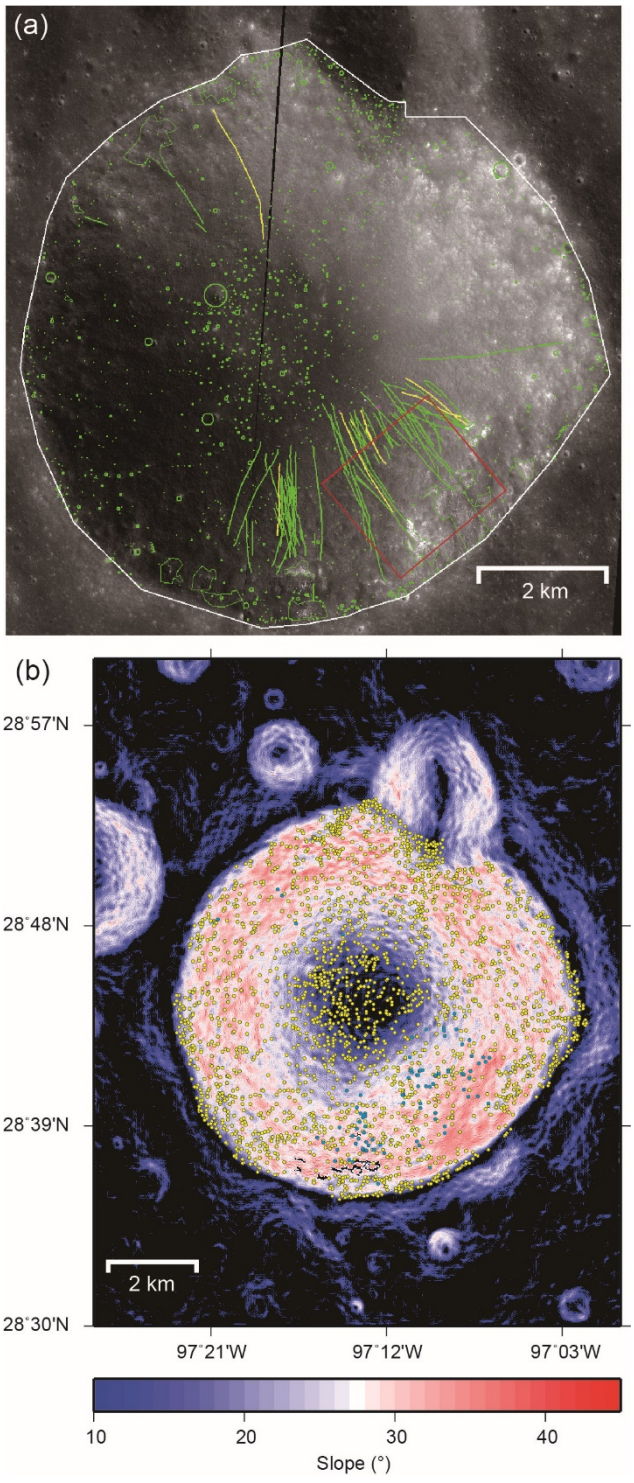
(a)
2 km
(b)
28°57'N
28°48'N
28°39'N
28°30'N
2 km
97°21'W
97°12'W
97°03'W
10
20
30
40
Slope (°)

Figure 6. (a) LROC NAC mosaic images (M1206659832RC and M1206659832LC) of Site 2 showing boulder sources (areas enclosed by green lines), boulder trails (green and yellow lines), and small craters ($D > 15$ m; red, yellow, and green circles, as in Figure 2a) in the study area (within the white line). (b) Slope angle distribution (color scale) estimated by using KAGUYA topographic data for Site 2 and the locations of small craters (yellow circles) and the starting points of boulder falls (cyan circles). The area within the red rectangle in (a) is discussed in Figure 7.

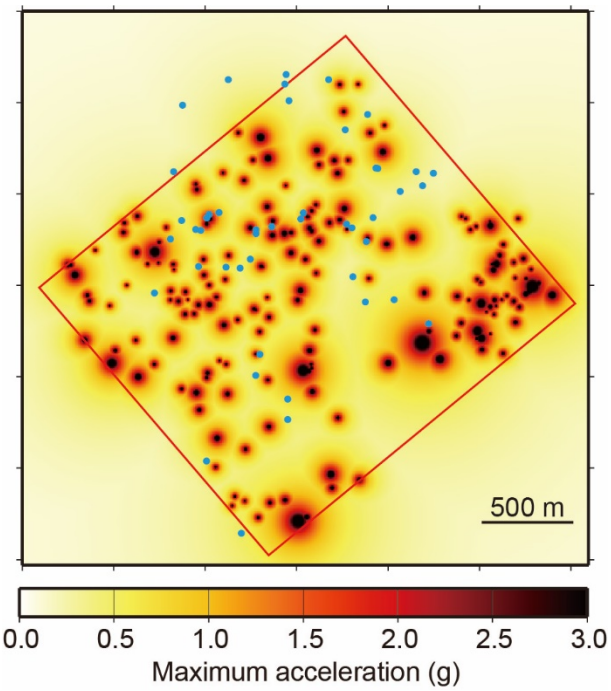

Figure 7. Spatial distributions of starting points of boulder falls (cyan circles) and maximum acceleration due to meteorite impacts (color scale) at Site 2 in and around the area within the red rectangle in Figure 6a.

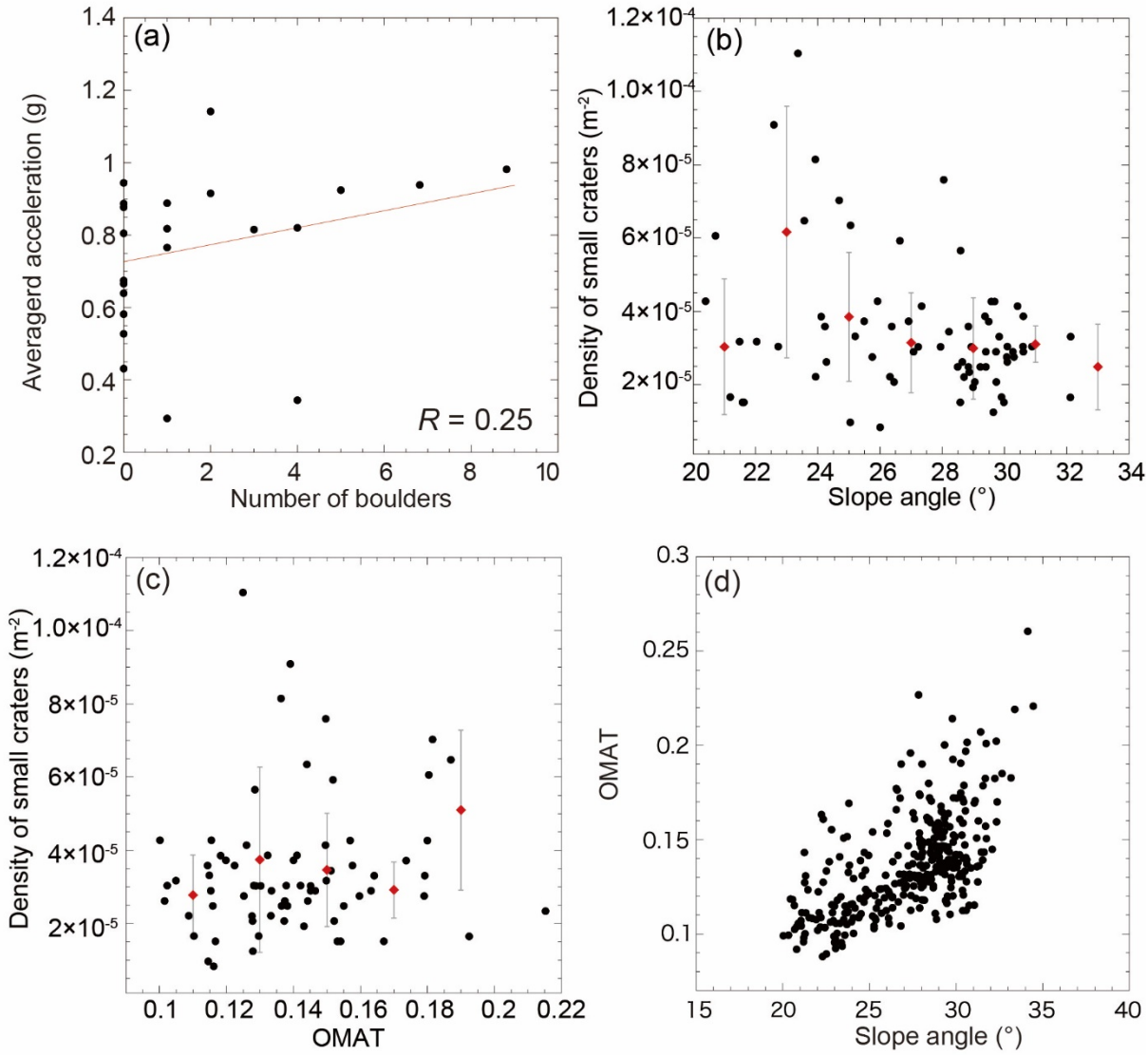

Figure 8. Relationships among various parameters at Site 2. (a) Averaged maximum acceleration versus the number of starting points of boulder falls with the best-fit linear relation (red line). (b) Density of small craters versus mean slope angle. (c) Density of small craters versus averaged OMAT values. (d) Mean slope angle versus averaged OMAT values. The study area was subdivided into grids with dimensions of 500 m × 500 m in (a), about 800 m × 900 in (b) and (c), and 400 m × 450 m in (d). Red diamonds and associated error bars in (b) and (c) show the averages and standard deviations of the density of small craters in the individual 2° slope angle bins and 0.02 OMAT bins, respectively.

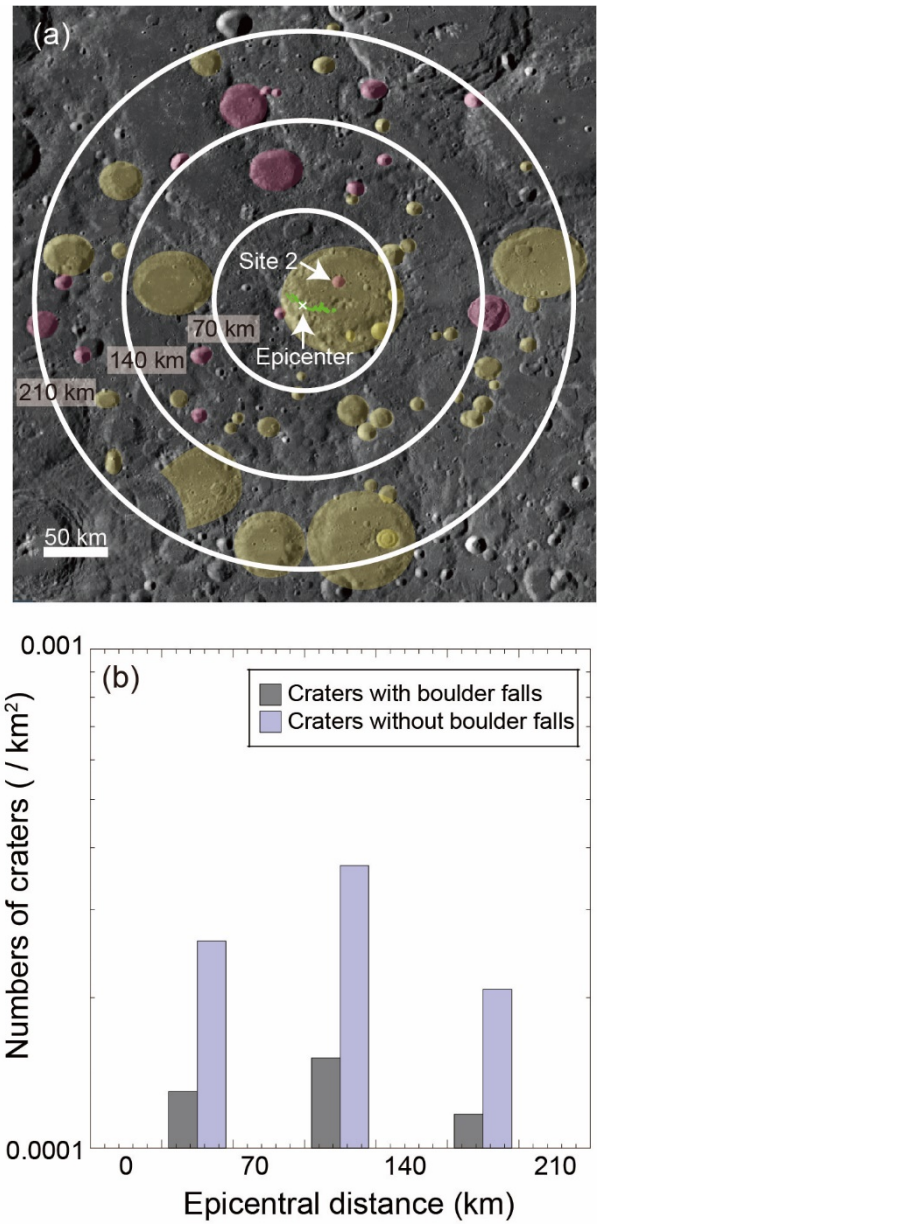

Figure 9. (a) Distribution of craters ($D > 7$ km) with (red fill) and without (yellow fill) boulder falls around Site 2. The epicenter of the moonquake on 3 January 1975 is shown by a white cross, and lobate scarps estimated by Kumar et al. (2019) are shown by green lines. (b) Histogram of the number of craters per unit area with and without boulder falls in relation to epicentral distance (see the text for details).

4. Discussion

We found the starting points of boulder falls to be spatially correlated with maximum ground acceleration due to meteorite impacts in region 2 at Site 1 (Figure 4a). This result strongly suggests that local ground shaking due to meteorite impacts triggered boulder falls in this region. Although we found no clear correlation in other regions at Site 1 (Figures S2b and S2d) or at Site 2 (Figure 8a), in these areas, boulder falls were not abundant, so statistical evaluation was difficult. The differences in the distribution of boulder falls may be due to differences in surface maturity, as is discussed below.

Kumar et al. (2019) estimated PGA values due to the moonquake on 3 January 1975 to be 1−4 g at Site 2 (epicentral distance about 30 km) and concluded that this moonquake along the lobate scarps triggered boulder falls at the site. Given such large acceleration, boulder falls should have been triggered not only at Site 2 but also in other craters, depending on epicentral distance. However, we found no dependence of the existence of craters with boulder falls on the distance from the epicenter of the moonquake (Figure 9). This result suggests that neither the boulder falls at Site 2 nor those in other craters around Site 2 were caused by ground shaking due to this moonquake.

Kumar et al. (2019) used the omega-square source model (e.g., Aki & Richards, 2002) to simulate seismograms stochastically, and half-space structural models of S-wave velocity and density with Q_i = 4000−15,000, in which scattering attenuation was not explicitly included. They assumed an S-wave velocity of 330 m/s, corresponding to the uppermost regolith layer in a half-space model. Such a very small S-wave velocity without scattering attenuation can result in large acceleration. We estimated PGA at Site 2 due to this moonquake by using the attenuation equation (equation (3)) to be about 0.1 g, which is an order of magnitude smaller than the estimates of Kumar et al. (2019). Our result suggests that the moonquake may have not caused large acceleration, although our PGA estimate may be problematic because of differences in Q_i and Q_s structures between the Moon and Earth, as we mention in Section 2.

The mean model ages estimated at Sites 1 and 2 (5.5 and 23 Ma, respectively) (Figures S1a and S5a) are clearly younger than the formation ages of the Schrödinger basin (Imbrian period) and Laue crater (Pre-Nectarian period or later) (Wilhelms, 1987). Therefore, craters on slopes at these sites have presumably been erased by subsequent mass-wasting processes. Older boulder trails superimposed by small impact craters and younger trails that crosscut craters are found at both sites (Figures 2a and 6a). Therefore, the boulder falls were not simultaneous but occurred repeatedly as a result of local ground shaking. Such repeated shaking is more likely to be produced by meteorite impacts than by moonquakes shaking a broad area.

The large OMAT values in the upslope boulder source areas at both sites (Figures 4d and 8d) indicate that immature surfaces are exposed in these areas. According to our age estimates, Site 2 is older than Site 1; furthermore, the area

with immature surfaces is smaller at Site 2 than at Site 1 (Figure 5). These findings suggest that surface degradation at Site 2 is more advanced than at Site 1. The more abundant boulder falls at Site 1 than at Site 2 (Figures 2a and 6a) reflect the existence of more boulders in the source areas at Site 1 than at Site 2. These boulders may have been produced by continuous fracturing, which may also expose immature surfaces. According to Basilevsky et al. (2013), who studied boulder survival times, the number of boulders larger than 2 m would be halved in tens of millions of years. Given the ages of the two sites, more boulders would have been destroyed at Site 2, and we found fewer boulders at Site 2 than at Site 1. At Site 1, we found more boulder falls in region 2 than in regions 1 and 3 (Figures 2a and S2). Our determinations of crater ages in regions 1–3 at Site 1 (7.5, 4.4, and 5.4 Ma, respectively) indicate that region 2 is youngest (Figure S1b). This result also supports our inference that the boulder source area is inversely related to age.

The correlation between boulder falls and acceleration due to meteorite impacts in region 2 at Site 1 and the lack of a clear dependence of boulder falls around Site 2 on moonquake epicentral distance suggest that boulder falls were not triggered by moonquakes along lobate scarps but by meteorites that repeatedly struck crater slopes and generated small craters.

Our finding that the density of small craters decreases with increasing slope angle at both Sites 1 and 2 (Figures 4b and 8b) is consistent with results obtained by Basilevsky (1976) for other craters. We also found that the density of small craters decreases with increasing OMAT values at Site 1 (Figure 4c), although a similar tendency was not clear at Site 2 (Figure 8c). We further found that OMAT values increase with increasing slope angle at both sites (Figures 4d and 8d). We note that small craters and boulder falls are rare in the areas below the boulder sources at Site 1 (areas enclosed by blue lines in Figure 2a) where the OMAT values are relatively small (Figure 5a).

Considering all of these results, we propose a mass-wasting model for the slopes at Sites 1 and 2 as follows. A surface regolith layer overlying the bedrock, consisting of brecciated rocks or megaregolith, was formed during the Late Heavy Bombardment (Hartmann, 1973). In steeply sloping areas, this surface layer is thin because fine regolith tends to move downward under the influence of gravity. Therefore, in such areas, the bedrock can be more easily fractured by meteorite impacts, which produce rock fragments and boulders and, therefore, boulder source areas (Figure 10a). These boulders move downward when ground shaking due to meteorite impacts occurs (Figure 10a). In steeply sloping areas, however, craters are not clearly visible because the surface regolith layer is thin, and if boulder falls occur, they do not leave clear trails. Furthermore, fresh regolith generated upslope moves downward and tends to erase boulder trails and small craters in areas below boulder sources. In gently sloping downslope areas, accumulation of regolith from upslope causes the surface layer to become thicker and older (Figure 10b). When meteorites strike these areas and trigger boulder falls, clear craters and boulder trails can be formed in the thick regolith layer

(Figure 10b). Repetition of these processes, however, makes the slope gentler and the surface layer thicker and results in the degradation of the crater wall (Figure 10c), and eventually, meteorite impacts no longer produce boulders and boulder trails.

This model consistently explains the distributions of boulder sources (Figure 5), boulder trails (Figures 2a and 6a), small craters (Figures 2b and 6b), and OMAT values (Figure 5) at Sites 1 and 2. Moreover, the differences in their distributions among regions 1−3 at Site 1, whose ages vary between 4.4 and 7.5 Ma, suggest that the processes described by our model can occur relatively rapidly, over about a million years. In addition, the weak relationships between ground acceleration and boulder abundance (Figure 8a) and between small crater density and slope angle (Figure 8c) at Site 2 (age 23 Ma) suggest that crater wall degradation at this site is advanced and implies that complete degradation can occur in a few tens of millions of years.

Previous crater degradation models (e.g., Ross, 1968; Fassett & Thomson, 2014) take account of redistributions of ejecta generated by meteorite impacts by using the diffusion equation to explain crater topography. In future studies, the boulder and regolith transport on crater walls described by our model should be quantitively examined to extend these previous models. According to Fassett and Thomson (2014), the diffusion equation does not well explain the topographic features of crater rims, which may be related instead to our proposed processes.

The results of this study suggest that boulder falls at Sites 1 and 2 were caused by meteorite impacts. Bickel et al. (2020, 2021) also proposed meteorite impacts produced boulders from rocks that had been fractured in the Late Heavy Bombardment. Although our model is similar to their concept, we examined in detail boulder generation processes by meteorite impacts in upslope areas with thin surface regolith layers. Furthermore, we provide a complete crater degradation model that accounts for boulder generation, boulder falls, and regolith movement. Bickel et al. (2020, 2021) also showed that boulder falls can be found over the entire lunar surface. In future studies, the universality of our mass-wasting model should be evaluated by investigating boulder sources, boulder trails, small carters, and OMAT values in other areas. The effects of shallow moonquakes should also be investigated in such areas. Comprehensive studies of the cause of boulder falls would contribute to better understanding of mass wasting related to the formation and degradation of lunar craters and new insights into ongoing dynamic activities on the lunar surface.

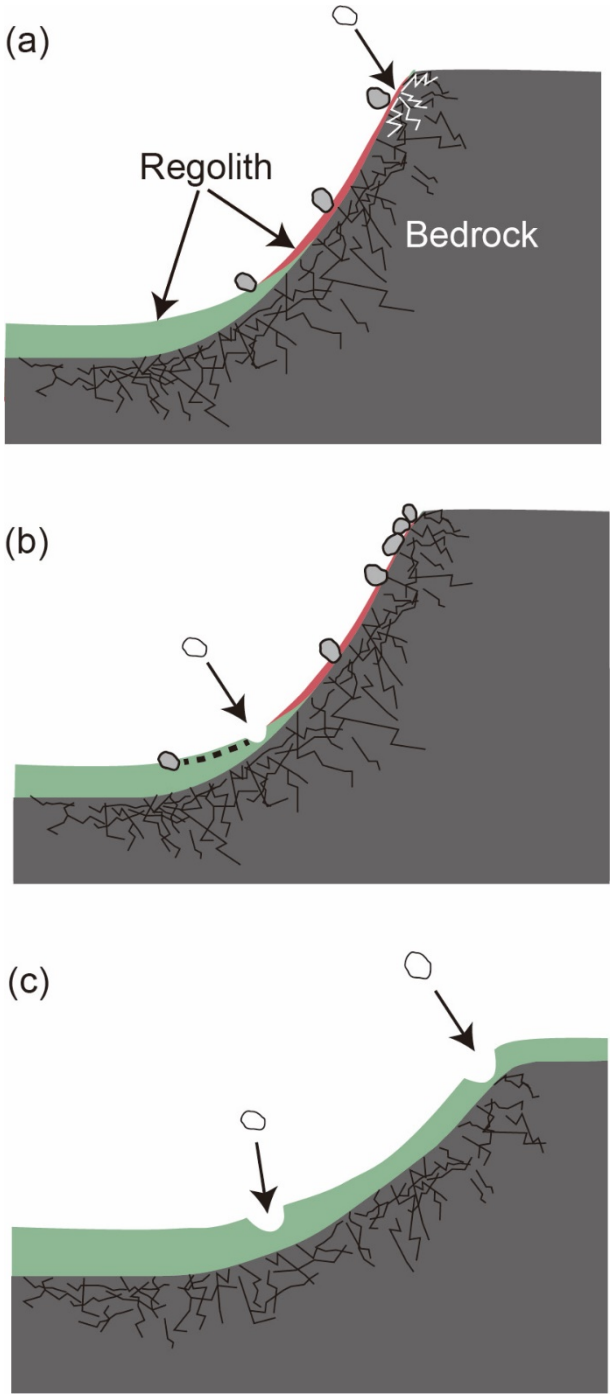

Figure 10. Schematic diagram of our mass-wasting model for Sites 1 and 2.

Older and younger regolith layers are shown by green and red, respectively. (a) In upslope areas, the surface regolith layer is thin, and boulders are more easily generated by meteorites striking the megaregolith bedrock. (b) Younger regolith generated in upslope regions moves downward by lunar gravity, and ground shaking caused by meteorite impacts triggers boulder falls. The resulting craters and boulder trails are clear in the thick regolith layer in gently sloping areas. (c) Repetition of the processes shown in (a) and (b) makes the slope gentler and the surface layer thicker and eventually results in the degradation of the crater wall.

5. Conclusions

We investigated the distributions of boulder sources, boulder trails, small craters, and OMAT values at Site 1 in the Schrödinger basin and Site 2 in Laue crater and found the following features: (1) boulder sources are located in upslope areas, and some boulder trails are superimposed by craters whereas other crosscut craters; (2) there are few small craters and boulder trails in areas with large slope angles; and (3) OMAT values are high in boulder source areas. Our estimated ages of the slopes at both Sites 1 and 2, based on small crater density, are clearly younger than the formation ages of the Schrödinger basin and Laue crater. Therefore, craters have been erased from these slopes by subsequent mass-wasting processes. The correlation between starting points of boulder falls and maximum acceleration due to impacts at Site 1 suggests that boulder falls were triggered by ground shaking caused by meteorite impacts. A moonquake on 3 January 1975 was thought to trigger boulder falls at Site 2. However, the distributions of craters with and without boulder falls within an epicentral distance of about 200 km showed no dependence on epicentral distance. Therefore, boulder falls at and around Site 2 were not triggered by the moonquake. Using our estimates of the density of small craters, slope angles, and OMAT values, we proposed a mass-wasting model for slopes at Sites 1 and 2 as follows: Meteorite impacts fracture the megaregolith bedrock in upslope areas where the surface regolith layer is thin, thereby producing boulder sources. Ground shaking due to meteorite impacts causes the boulders to move down the slopes; boulder trails and small impact craters are clearly visible in downslope areas, where regolith derived from upslope areas has caused a thick regolith layer to accumulate. Repetition of these processes makes the slopes gentler and the surface regolith layer thicker, and results in degraded craters without boulder falls. The results of this study strongly suggest that boulder falls in these areas are not caused by shallow moonquakes along lobate scarps but by ground shaking due to meteorite impacts. In future studies, the distributions of boulder falls, boulder sources, small craters, and OMAT values should be systematically investigated in other areas to evaluate the universality of the mass-wasting model proposed by this study.

Acknowledgments

We thank Sei-ichiro Watanabe, Sinichi Sirono, and Hiroaki Katsuragi for useful comments and discussions. This work was partly supported by Nagoya Univer-

sity Interdisciplinary Frontier Fellowship and JSPS KAKENHI grant 20H00194.

Data Availability Statement

The NAC image data are available at https://wms.lroc.asu.edu/lroc/search by entering the image names listed in Table 1 (M154370363LC, M1097122291LC, M1390708014LC, M1244314600RC, M141446269LC, M1206659832RC, M139071213LC, and M1206659832LC) into the "Product ID" field. The MI and DEM data are available at https://darts.isas.jaxa.jp/planet/pdap/selene/product_search.html by entering "SELENE MOON MI 5 MAP V3.0" and "SELENE MOON TC 5 DTM MAP SEAMLESS V2.0" into the "Data set name" field, respectively, with latitude and longitude ranges shown in the image names in Table 1. Our estimated data of small craters, boulder trails, and boulder sources, densities of small craters, and OMAT values can be found online (https://1drv.ms/u/s!Au3OlkoCl34TalfovoJGus7iNoY?e=g499Kv). This link is for the peer review only, and the data will be reposited in the Harvard Dataverse (https://dataverse.harvard.edu) after the acceptance of this manuscript.

References

Aki, K., & Richards, P.G. (2002). *Quantitative Seismology* (2nd ed.). Sausalito, CA: University Science Books.

Araki, H. Tazawa, S., Noda, H., Ishihara, Y., Goossens, S., Sasaki, S., et al. (2009). Lunar global shape and polar topography derived from Kaguya-LALT laser altimetry, *Science*, 323 (5916), 897−900. https://doi.org/10.1126/science.1164146.

Basilevsky, A. T. (1976). On the evolution rate of small lunar craters, In *Proceedings of the Lunar and Planetary Science Conference*, 7th, 1005–1020.

Basilevsky, A.T., Head, J.W., & Horz, F. (2013). Survival times of meter-sized boulders on the surface of the Moon, *Planetary and Space Science*, 89, 118–126. http://dx.doi.org/10.1016/j.pss.2013.07.011.

Bickel, V. T., Aaron, J., Manconi, A., Loew, S., & Mall, U. (2020). Impacts drive lunar rockfalls over billions of years, *Nature communications*, 11 (2862). https://doi.org/10.1038/s41467-020-16653-3

Bickel, V. T., Aaron, J., Manconi, A., & Loew, S. (2021). Global Drivers and Transport Mechanisms of Lunar Rockfalls. *Journal of Geophysical Research: Planets*, Planets, 126, e2021JE006824. https://doi.org/10.1029/2021JE006824

Dziewonski, A. M., & Anderson, D. L. (1981). Preliminary reference Earth model. *Physics of the Earth and Planetary Interiors*, 25, 297−356. https://doi.org/10.1016/0031-9201(81)90046-7

Fassett, C. I., & Thomson, B. J., (2014). Crater degradation on the lunar maria: Topographic diffusion and the rate of erosion on the Moon. *Journal of Geophysical Research: Planets*, 119, 2255–2271. https://doi.org/10.1002/2014JE004698

Hartmann, W. K. (1973). Ancient lunar mega-regolith and subsurface structure. *Icarus*, 18, 634−636. https://doi.org/10.1016/0019-1035(73)90066-3

Haruyama, J., T. Matsunaga, M. Ohtake, T. Morota, C. Honda, Y. Yokota, M. Torii, Y. Ogawa, and the LISM Working Group (2008), Global lunar-surface mapping experiment using the lunar imager/spectrometer on SELENE, Earth Planets Space, 60, 243–255, doi:10.1186/BF03352788.

Head III, J. W., Fasset, C. I., Kadish S. J., Smith, D. E., Zuber, M. T., Neumann, G. A., & Mazarico, E., (2010). Global distribution of large lunar craters: Implications for resurfacing and impactor populations. *Science* 329, 1504–1507. https://doi.org/10.1126/science.1195050

Houston, W. N., Moriwaki, Y., & Chang. C. S. (1973). Downslope movement of lunar soil and rock caused by meteoroid impact. In *Proceedings of the Lunar and Planetary Science Conference,* 3(4), 2425−2435.

Joye, W. A, & Mandel. E. (2003). New features of SAOImage DS9. *Astronomical Data Analysis Software and Systems XII ASP Conference Series*, 295, 489−492.

Kanamori, H. (1977). The energy release in great earthquakes. *Journal of Geophysical Research*, 82, 2981−2987.

Kanno, T., Narita, A., Morikawa, N., Fujiwara, H., & Fukushima. Y. (2006). A new attenuation relation for strong ground motion in Japan based on recorded data, *Bulletin of the Seismological Society of America*, 96(3), 879–897. https://doi.org/10.1785/0120050138

Kokelaar, B.P., Bahia, R. S., Joy, K. H., Viroulet, S., & Gray, J. M. N. T. (2017). Granular avalanches on the Moon: Mass-wasting conditions, processes, and features, *Journal of Geophysical Research Planets*, 122, 1893–1925. https://doi.org/10.1002/2017JE005320

Kumar, P. S., Sruthi, U., Krishna, N., Lakshmi, K. J. P., Menon, R., Amitabh, et al. (2016). Recent shallow moonquake and impact-triggered boulder falls on the Moon: New insights from the Schrödinger basin. *Journal of Geophysical Research Planets*, 121, 147–179. https://doi.org/10.1002/2015JE004850

Kumar, P. S., Mohanty, R., Lakshmi, K. J. P., Raghukanth, S. T. G., Dabhu, A. C., Rajasekhar, R. P., & Menon, R. (2019). The seismically active lobate scarps and coseismic lunar boulder avalanches triggered by 3 January 1975 (M_W 4.1) shallow moonquake. *Geophysical Research Letters*, 46, 7972–7981. https://doi.org/10.1029/2019GL083580

Lucey, P. G., Taylor, G. J., & Malaret. E. (1995). Abundance and distribution of iron on the Moon. *Science*, 268(5214), 1150−1153. https://doi.org/10.1126/science.268.5214.1150

Lucey, P. G., Blewett, D. T., Taylor, G. J., & Hawke., B. R. (2000). Imaging

of lunar surface maturity. *Journal of Geophysical Research Planets*, 105, 20377–20386. https://doi.org/10.1029/1999JE001110

Michael G.G., & Neukum G. (2010). Planetary surface dating from crater size-frequency distribution measurements: Partial resurfacing events and statistical age uncertainty, *Earth and Planetary Science Letters*, 294 (3-4), 223-229. https://doi.org/10.1016/j.epsl.2009.12.041

Mohanty, R., Kumar, P. S., Raghukanth, S. T. G., & Lakshmi, K. J. P. (2020). The long-lived and recent seismicity at the lunar Orientale basin: Evidence from morphology and formation ages of boulder avalanches, tectonics, and seismic ground motion. *Journal of Geophysical Research: Planets*, 125, e2020JE006553. https://doi.org/10.1029/2020JE006553

Nakamura, Y., & Koyama, J. (1982). Seismic Q of the lunar upper mantle. *Journal of Geophysical Research: Solid Earth*, 87(B6), 4855-4861. https://doi.org/10.1029/JB087iB06p04855

Nakamura, Y., Latham, G. V., Dorman, H. J., Ibrahim, A. K., Koyama, J., & Horvath, P. (1979). Shallow moonquakes: Depth, distribution and implications as to the present state of the lunar interior. In *Proceedings of the Lunar and Planetary Science Conference,* 2299–2309.

Neukum, G. (1983). Meteoritenbombardement und Datierung planetarer Oberflächen, Habilitation Dissertation for Faculty Membership. Ludwig-Maximilians-Univ, Munich.

Neukum, G., Ivanov, B. A., & Hartmann, W. K. (2001), Cratering in the inner solar system in relation to the lunar reference system. Chronology and Evolution of Mars, 96, 55−86.

Ohtake, M., Matsunaga, T., Haruyama, J., Yokota, Y., Morota, T., Honda, C., et al. (2009). The global distribution of pure anorthosite on the Moon. *Nature*, 461, 236−240. https://doi.org/10.1038/nature08317

Otake, H., Ohtake, M., & Hirata, N. (2012). Lunar iron and titanium abundance algorithms based on SELENE (KAGUYA) multiband imager data. 43rd *Lunar and Planetary Science Conference* XLIII, Abstract 1905.

Robinson, M.S., Brylow, S. M., Tschimmel, M., Humm, D., Lawrence, S. J. Thomas, P. C. et al., (2010). Lunar Reconnaissance Orbiter Camera instrument overview. Space Science Reviews, 150, 81–124, doi:10.1007/s11214- 010-9634-2.

Robinson, M. S., Aaron, K. B., Brett, W. D., Samuel, J. L., Alfred, S. M., Danielle, E. M., et al. (2015). New crater on the Moon and a swarm of secondaries. *Icarus*, 252, 229−235. https://doi.org/10.1016/j.icarus.2015.01.019

Ross, H. P. (1968). A simplified mathematical model for lunar crater erosion, *Journal of Geophysical Research*, 73, 1343–1354. https://doi.org/10.1029/JB073i004p01343

Sato, H., Fehler, C. M., & Maeda, T. (2012). *Seismic wave propagation and scattering in the heterogeneous earth* (2nd ed.). Springer-Verlag.

Teanby, N. A., & Wookey, J. (2011). Seismic detection of meteorite impacts on Mars. *Physics of the Earth and Planetary Interiors*, 186, 70–80. https://doi.org/10.1016/j.pepi.2011.03.004

Tera, F., Papanastassiou, D. A., & Wasserburg, G. J. (1974). Isotopic evidence for a terminal lunar cataclysm. *Earth and Planetary Science Letters*, 22, 1–21. https://doi.org/10.1016/0012-821X(74)90059-4

Watters, T. R., Robinson, M. S., Beyer, R. A., Banks, M. E., Bell III, J. F., Pitchard, M. E., et al. (2010). Evidence of recent thrust faulting on the Moon revealed by the Lunar Reconnaissance Orbiter Camera. *Science*, 329(5994), 936−940. https://doi.org/10.1126/science.1189590

Watters, T. R., Robinson, M. S., Collins, G. C., Banks, M. E., Daud, K., Williams, N. R., & Selvans, M. M. (2015). Global thrust faulting on the Moon and the influence of tidal stresses. *Geology*, 43(10), 851–854. https://doi.org/10.1130/G37120.1

Watters, T. R., Weber, R. C., Collins, G. C., Howley, I. J., Schmerr, N. C., & Johnson, C. L. (2019). Shallow seismic activity and young thrust faults on the Moon. *Nature Geoscience*, 12, 411–417. https://doi.org/10.1038/s41561-019-0362-2

Wessel, P., & Smith, W. H. F. (1998). New, improved version of Generic Mapping Tools released. *EOS Transaction AGU*, 79, 579. https://doi.org/10.1029/98EO00426

Wilhelms, D. E. (1987). *The Geologic History of the Moon*, U.S. Geological Survey Professional Paper 1384. United States Government Printing Office. https://doi.org/10.3133/pp1348

Xiao, Z., Z. Zeng, N. Ding, and J. Molaro. (2013), Mass wasting features on the Moon—How active is the lunar surface? *Earth and Planetary Science Letters*, 376, 1–11. https://doi.org/10.1016/j.epsl.2013.06.015